Photon Tunneling Microscopy of Polymeric Surfaces

John M. Guerra, Mohan Srinivasarao, Richard S. Stein

With photon tunneling microscopy it is possible to image polymeric and other dielectric surfaces by means of the unusual properties of photon tunneling or evanescent waves. Vertical resolution is 1 nanometer, limited by the detector, over a vertical range of half a wavelength. Lateral resolution is better than a quarter of a wavelength over a field of view up to 125 micrometers. Samples can be surveyed in real time in air, with no need for metallization, and without shadowing or the intrusive effects of electrons or scanning probes. The use of this technique to study single crystals of polyethylene and processes such as latex film formation and the evolution of polystyrene topography while dewetting above the glass transition temperature are described.

In many of the numerous applications of polymers, such as paints, optical coatings, industrial substrates, medical implants, clothing, and even ivory substitutes on piano keys, surface topography influences the performance (optical, mechanical, thermal, electrical, and so on), appearance, wear, and adhesion of the materials (*1, 2*). In this article, we highlight the advantages that photon tunneling microscopy (*3*) brings to the study of polymer surface topography and illustrate them with a report on some representative imaging applications.

Researchers today have available a powerful arsenal of microscopes, from the low-voltage and environmental scanning electron microscopes (SEMs) to the new and growing family of scanning probe microscopes (SPMs) (*4–9*) initiated by the scanning tunneling microscope (STM) (*10*). Light microscopy, including dark-field, polarized (*11*), reflected light, spectroscopic, fluorescence, and interference techniques (*12*), continues to be the workhorse of polymer imaging because it provides direct, visual, whole-field and real-time imaging of the unperturbed surface. Samples are accessible, easily explored and moved, and interference allows topography to be measured [for example, lamellae thicknesses of polymer crystals (*12*)]. Information is gathered in a parallel manner, rather than serially, as with scanning methods. Imaging is therefore fast, which allows large sample surveys and redundant imaging for high data confidence, as well as imaging of dynamic samples. The typical low-energy light can be spectrally modified to eliminate sample modification, as when imaging a photoresist.

Light microscopy has undergone great evolution. The phase-modulated interference microscope produces topographic images and height quantification with high vertical resolution over a large vertical range, although not at present, in real time (*13*). The more recent confocal microscope (*14*) incorporates serial scanning into the light microscope to increase the lateral resolution and, in addition to topographic imaging, can be used to construct tomographic images of biological and other samples.

The photon tunneling microscope (PTM), another extension of light microscopy, only became available commercially in 1992, although it has been in proprietary service since 1985 (*15, 16*). The PTM descends from frustrated total internal reflection microscopy (*17*) or from evanescent wave or surface contact microscopy (*18*) when used in the transmission mode. The direct visual tunneling images are also displayed as real-time, topographic, three-dimensional (3D) images, with continuously variable viewpoint and magnification control. Single profiles are isolated for video cross-sectioning of the sample. Because the PTM is a light microscope, it can be configured for spectroscopic, fluorescence, surface plasmon (*19*), polarization, and other studies, in transmission as well as the normal reflection mode.

Brief Description of the PTM

The PTM, like its forebear, is based on the behavior of light at the boundary between a dielectric medium 1 with index of refraction η_1 and dielectric medium 2 with a lesser index of refraction η_2. Total internal reflection (TIR) occurs in medium 1 if the angle of incidence θ is equal to or greater than the critical angle $\sin^{-1}(\eta_2/\eta_1)$. Probing the rarer medium near the TIR surface with a dielectric surface of η_3 greater than η_2 couples energy from the first medium (Fig. 1), indicating the presence in the rarer medium of an electromagnetic wave, as first observed by Newton (*20*). It has the same frequency as its parent wave in the denser medium and is evanescent because it does not carry any energy from the TIR surface in averaged time if unperturbed.

For homogeneous transparent dielectric media, the field strength of the evanescent wave decays exponentially as $E_0 \exp(-z/d_p)$, where z is the distance normal to the TIR boundary and d_p is the penetration depth into medium 2 at which the field strength falls to $1/e$ of its initial value E_0

$$d_p = \frac{\lambda_1}{2\pi(\sin^2\theta - \eta_{21}^2)^{1/2}}$$

where $\eta_{21} = \eta_2/\eta_1$ and λ_1 is the illumination wavelength in medium 1 (Fig. 1).

Evanescent waves are fully explained by classical optics (*21–23*), but ideas from quantum theory add to the intuitive understanding of the microscopy. The analogy to electron barrier tunneling has been elegantly made (*24–28*), and the effect is known as optical or photon tunneling. The exponential decay then represents the probability of encountering a photon from medium 1 in the tunneling gap at some distance z normal to the TIR boundary.

Photon tunneling has several remarkable properties of significance to microscopy:

The exponential decay of the tunneling probability encodes height information in the sample topography into a gray-scale tunneling image, the photometry of which yields profilometry directly after empirical calibration. The smoothly continuous decay of the tunneling probability frees vertical resolution from wavelength constraints; vertical resolution is limited in practice by photometric resolution, determined by the signal-to-noise ratio of the detector (which also affects the vertical range).

Photons tunneling into the gap are the same frequency as in medium 1, so that the high lateral resolution of oil immersion microscopy is achieved even though the sample remains dry. In addition, only light at and beyond the critical angle in medium 1 is totally internally reflected, so the illumination forming the photon tunneling

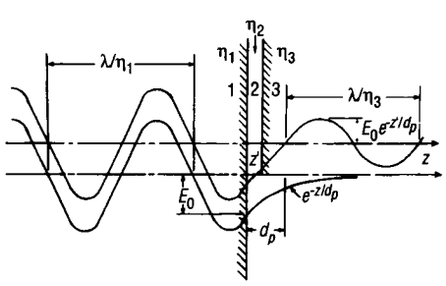

Fig. 1. Schematic diagram showing the energetics and geometry of photon tunneling.

J. M. Guerra is in the Optical Engineering Division, Polaroid Corporation, Cambridge, MA 02139. M. Srinivasarao and R. S. Stein are at the Polymer Research Institute, University of Massachusetts, Amherst, MA 01003.

image is annular. This enhances the higher spatial frequencies, amplifying lateral resolution by 1.3 to 1.6 times (*29–31*). Such enhanced resolution is common to optical systems with centrally obstructed apertures and is used to advantage in applications from microlithography to astronomy. The full numerical aperture (NA) nevertheless remains available for imaging the sample.

Evanescent waves generated in turn by the illuminated sample's microfeatures (*32*) are received and converted by the proximal transducer into propagating image-forming light, leading to a "super numerical aperture" where collection of the evanescent waves normally missed in a light microscope results in higher lateral resolution. There may also be contributions to the resolution from evanescent waves generated by the microroughness of the transducer itself, and this is being explored.

The inherent high contrast of the gray-scale tunneling image, going from dark to light (TIR) over a vertical range of only $\lambda/2$, helps the system modulation transfer function (MTF) (the optical as well as video resolution chain).

These properties lead to light microscope profilometry with nanometer vertical resolution and lateral resolution better than $\lambda/4$. The latter is a true resolution value derived from an Abbe-type periodic target (*33*) rather than a visibility limit.

Finally, the coherence of the microscope is intentionally kept low by use of the full NA of the objective and use of broadband filters in the illumination, with no restriction on polarization. This not only improves the lateral resolution but also adjusts the system linearity for highest topographic fidelity and makes the tunneling response more tolerant of optical variations if present in the sample (*3*).

Instrumentation. Configuring a reflected light microscope for photon tunneling is straightforward, requiring only TIR of the epi-illumination at a surface in the object plane. The objective is oil immersed to a transparent window, or transducer, and focused on its distal surface (Fig. 2). The NA of the objective is larger than one to contain the critical angle defined by the refractive indices of the transducer and the tunneling gap, so that TIR occurs at the transducer's distal surface. Accordingly, an aqueous tunneling gap, as with in vivo biological samples, requires the NA to be greater than 1.33. For high index transducers that are hemispherical rather than planoparallel, the required NA can be less than unity.

For photon tunneling to occur, the sample is placed in proximity to the transducer (so called because in this configuration, the window facilitates conversion of height modulation in the sample topography into light modulation) before oil immersion to the objective (the sample remains dry). In addition to providing the required optical unity for TIR (partially frustrated now by local photon tunneling into the sample), the immersion oil between the transducer and the objective allows the sample and transducer to travel together with respect to the microscope. This eliminates damaging sliding contact, protects the sample from the oil, and allows complete freedom of movement about the surface.

A recent innovation is a proprietary (Polaroid Corp.) flexible transducer. It is stiff and flat over the field of view of the microscope but flexible enough on a larger scale to accommodate curved surfaces and even dirt on the sample. It can be made large enough to cover and protect any sample, can be coated for surface plasmon studies, and height features for calibration or other uses, such as control of the tunneling gap, can be embossed into it.

The vertical tunneling range is about $\lambda/2$, or 0.3 μm for red light. Where the gap grows larger than this and the tunneling image is lost for the deeper topography, the transducer serves as a soft contact interference reference, with only refocusing and suppression of TIR illumination required for interferometry.

The PTM gleans height information from the tunneling modulation caused by the (optically homogeneous) sample topography referenced to the transducer. This simple arrangement precludes the need for vertical control instrumentation and its limitation on vertical resolution (*32*), but to measure height (and not optical variation as in waveguides, latent images in photoresist, or biological samples), the photon tunneling response must be calibrated to the particular optical properties of the sample. There are several ways of doing this, but empirical calibration to identical material of known geometry, such as a spherical surface, allows the relation of sample height to the gray-scale tunneling image to be directly measured and also provides a check on optical homogeneity. Polymers that cannot be fashioned into a sphere are spin-coated onto a spherical substrate. Differences in film and bulk indices are rarely a problem because an ≈1% variation has the same effect on the tunneling image as a 1-nm variation in topographic height, which is just resolved with the present detector.

A photometric vidicon or charge-coupled device (CCD) views the tunneling image at the microscope's phototube in the normal manner. The CCD offers the better signal-to-noise ratio and therefore higher vertical resolution and vertical range (which in practice is the tunneling range divided by the number of resolvable gray levels), but the vidicon has higher lateral resolution at lower cost, and with a pasicon tube, the vertical resolution is about a nanometer. Fortuitously, the nonlin-

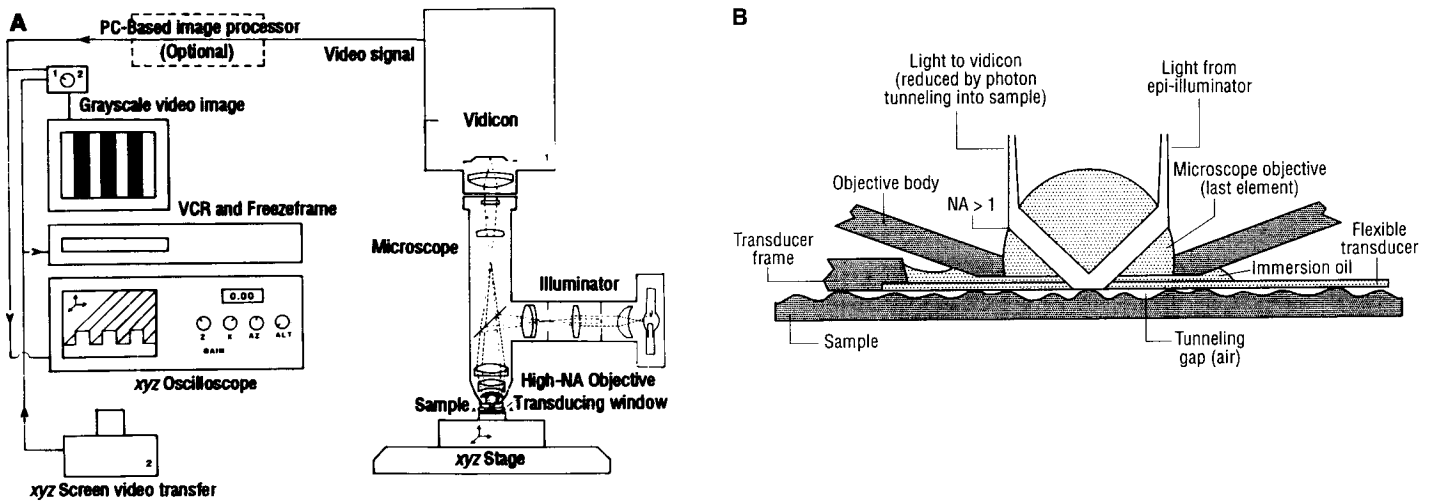

Fig. 2. Schematic diagram of (**A**) the photon tunneling microscope and (**B**) the transducer, objective, and sample.

ear response of the vidicon to intensity largely corrects the exponential response of tunneling to linear height, so that in the absence of image processing to correct the gray scale, the 3D display of the topography is true. Thus, the resolution is convolved with the detector characteristics, and detector tradeoffs must be considered.

The video signal can be analyzed and displayed in a number of ways, but at present, analog processing has the speed and resolution advantage over digital in the 3D display. A high-resolution *xy* oscilloscope displays each of the video raster lines as amplitude traces, thus electronically mapping intensity back into height for a real-time 3D image (*3*). Analog circuits shear, expand, or collapse the multiple oscilloscope amplitude traces to control 3D viewpoint with simple turns of a few knobs. A single trace can be isolated anywhere in the image for electronic cross-sectioning and height measurement.

Film Formation of Polymer Latex

Films formed from polymer latexes, and the mechanism of film formation, are of considerable industrial importance (*34–36*). Polymer latexes are water-based coating formulations containing the polymer as a colloidal suspension of spheres. When allowed to dry, some latexes produce transparent, continuous, crack-free, and mechanically rigid films, whereas some others give rise to opaque powders. Such differences arise from the latex particle size and the temperature at which the film was formed. Films formed above the minimum film-forming temperature (MFT) are usually transparent and continuous.

Several multistep mechanisms have been proposed in order to understand the film formation process and to account for the variables that affect the final film. The most widely accepted mechanism has three stages. First, the water evaporates, leading to close contact of particles. Second, it is believed that the particles pack and deform as water evaporates, giving structures [as examined by scanning and transmission electron microscopy (SEM and TEM, respectively)] consistent with face-centered-cubic (fcc) packing. Third, annealing the film at temperatures greater than the glass transition temperature T_g of the polymer latex leads to a mechanically rigid film. These stages and the respective temperature ranges depend on a number of parameters, which include the latex structure, size, and composition, as well as dispersion formulation.

We used 50-nm spheres (traceable to the National Institute of Standards and Technology) of polystyrene suspended in water. A drop of the suspension was air dried on a glass plate, leading to a film with very interesting surface topography. This film is rather turbid and is not mechanically rigid. Nomarski imaging (*12*) reveals a beautiful system of radial and tangential features (Fig. 3A). The gray-scale tunneling image from the PTM (Fig. 3B) shows these surface height variations and the additional diagonal features in high contrast, which when seen in 3D (Fig. 3, C and D), are revealed to be ridges running diagonally, with occasional orthogonal flipping across tiles defined by cracks. The flexible transducer was used in this case. These features are also seen in Nomarski imaging but are restricted to an overhead view, and with less resolution than with the PTM. The shift in the ridges across cracks indicate they were once continuous and formed before the cracking. Further, the cusping of the tile edges is obvious in a PTM. The spheres themselves are beyond the lateral resolution of the PTM, but structure is indicated.

It appears that the observed topography of the latex film is consistent with an incomplete close-packed structure for the latex particles. A detailed analysis of the structure formation below and above the MFT and in real-time is currently under way (*37*).

Imaging of Polymer Single Crystals

Many synthetic polymers can be crystallized from dilute solutions to form what are usually referred to as "polymer single crystals." The discovery in 1957 of such single crystals (*38–40*) has had a profound impact on the understanding of the crystallization and self-assembly of macromolecules (and recently, proteins). Electron diffraction data showed that the polymer chains (polyethylene) were normal to the crystal platelets formed from dilute solution. Remarkably, the platelets were only about 100 Å thick. This led Keller and O'Connor (*41*) to conclude that the molecules must fold sharply on themselves, giving rise to lamellar periods of only 100 Å. Since then, several studies have been carried out on solution-grown crystals (*42*).

For imaging with the PTM, polyethylene (Marlex-50) was crystallized from a dilute (0.5%) solution in *p*-xylene at 80°C to obtain large single crystals. A small amount of the suspension of single crystals in *p*-xylene was deposited on a microscope slide, and the solvent was removed by evaporation under atmospheric conditions. The flexible transducer was used in this application.

The gray-scale tunneling image of a polyethylene single crystal viewed directly in the PTM eyepiece (although the quality of this image is considerably reduced by the video chain) shows the individual lamella as intensity differences (Fig. 4A). The high resolution and contrast of this image are remarkable. The analog 3D display of the gray-scale image (Fig. 4B) clearly shows the individual lamellae of the polyethylene crystals, with step heights of ~70 Å. Ma-

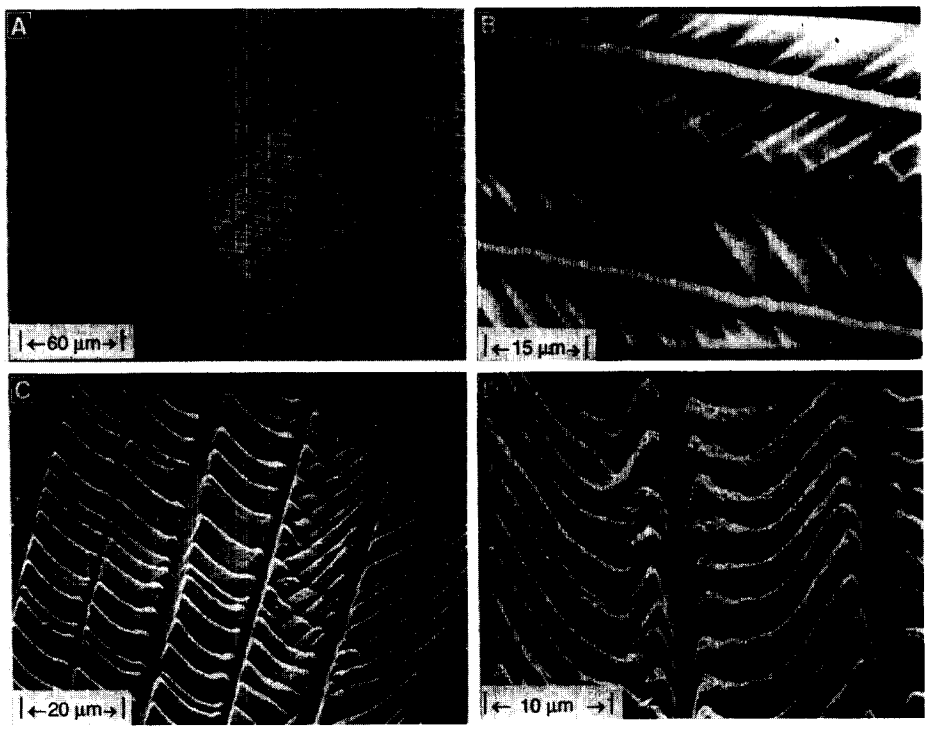

Fig. 3. (**A**) Nomarski image of the radial cracks formed when an emulsion of 50-nm latex spheres dries. (**B**) Gray-scale PTM image and (**C** and **D**) two 3D images of the same film.

nipulation of both the perspective and anamorphism in the 3D image helps to reveal the surface (Fig. 4C). The apparent height in the 3D image is exaggerated in comparison with the lateral dimensions. The long side of the image is 25 μm across, whereas as above, the step heights are only on the order of 70 to 80 Å.

Frequently, the topography of the single crystals exceeded the tunneling range because many of the crystals had a growth spiral center that was much thicker than the rest of the crystal. This lifted the flexible transducer beyond the tunneling range. In such a situation, one uses the microscope in the contact interference mode described earlier to image the thicker crystal. An interference image of a single crystal consisting of several lamellae was obtained with the PTM in the interference mode (Fig. 4D).

Dewetting Studies of Polystyrene

The processes of a liquid wetting a surface and a liquid film drying from a solid surface are important in many practical applications, for example, in paints and other coatings, detergents, and flow through porous media. In addition, thin polymer films are used in a variety of applications where their thermal stability is important; in many cases, a smooth and stable surface is desirable.

Wetting and dewetting of a liquid film on a solid surface depends on the nature of long-range interactions between the liquid and the solid. Wetting is reasonably well understood (*43–46*), and our experiments were designed to study the inverse process, that is, the retraction and rupture, or dewetting, of a thin polymer film on a glass substrate. A common example is the way a film of water that has been spread on a waxed automobile spontaneously ruptures and draws up into small beads.

It is possible with techniques like spin coating to prepare smooth surfaces of controlled thickness of polymer films even on nonwettable (defined by a nonzero contact angle between the substrate and the polymer film) surfaces. Films prepared on nonwettable surfaces, however, are not stable above their glass transition temperature and will rupture spontaneously, giving rise to beads of the polymer (*46*).

Experimental studies of thick films of a nonvolatile fluid dewetting (*47*) and of thin films (<100 nm) of polystyrene have been reported (*48*). Thick films undergo the dewetting process by a nucleation and growth mechanism (*47*), whereas thin films (<100 nm) are expected to undergo dewetting by means of a spinodal-type decomposition. Evidence for spinodal decomposition has been given (*48*) on the basis of the size of the droplets observed on completion of dewetting.

Our experiments were designed to directly observe the process that eventually ruptures the film, leading to droplets of size h^2/a, where h is the initial thickness of the film and a is a molecular size (*46*). Thin films of polystyrene (weight- and number-averaged molecular weights M_w = 19,000; M_w/M_n < 1.05; Polymer Laboratories, United Kingdom) were coated onto a glass substrate from dilute solutions of polystyrene in toluene. The concen-

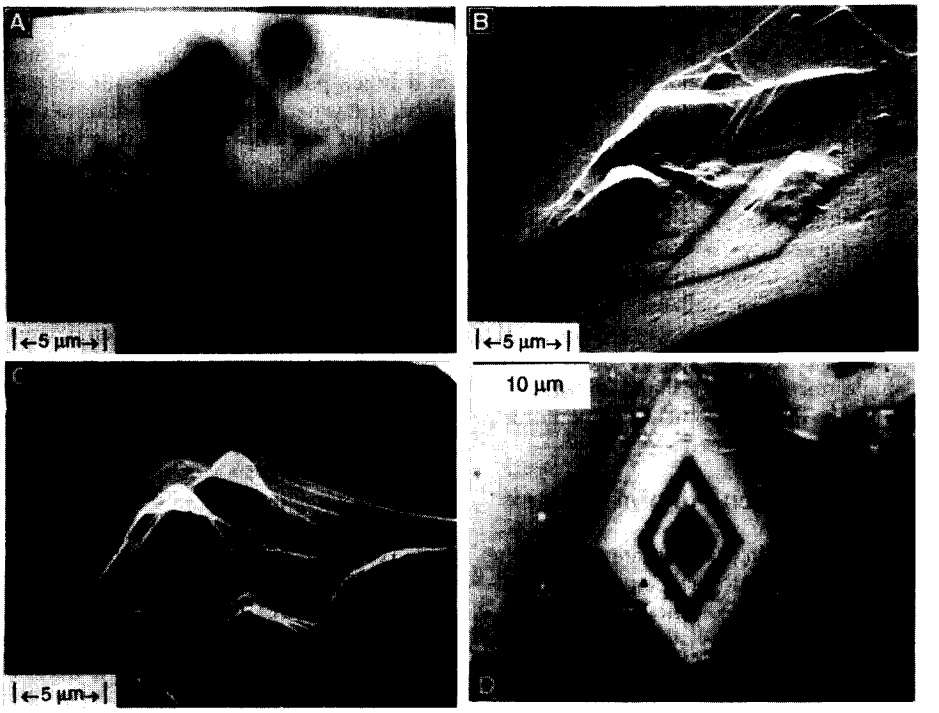

Fig. 4. (**A**) Gray-scale PTM image of single polyethylene crystals and (**B** and **C**) 3D images showing the topography from different viewpoints. (**D**) A single large crystal can be imaged with the PTM in contact interference mode.

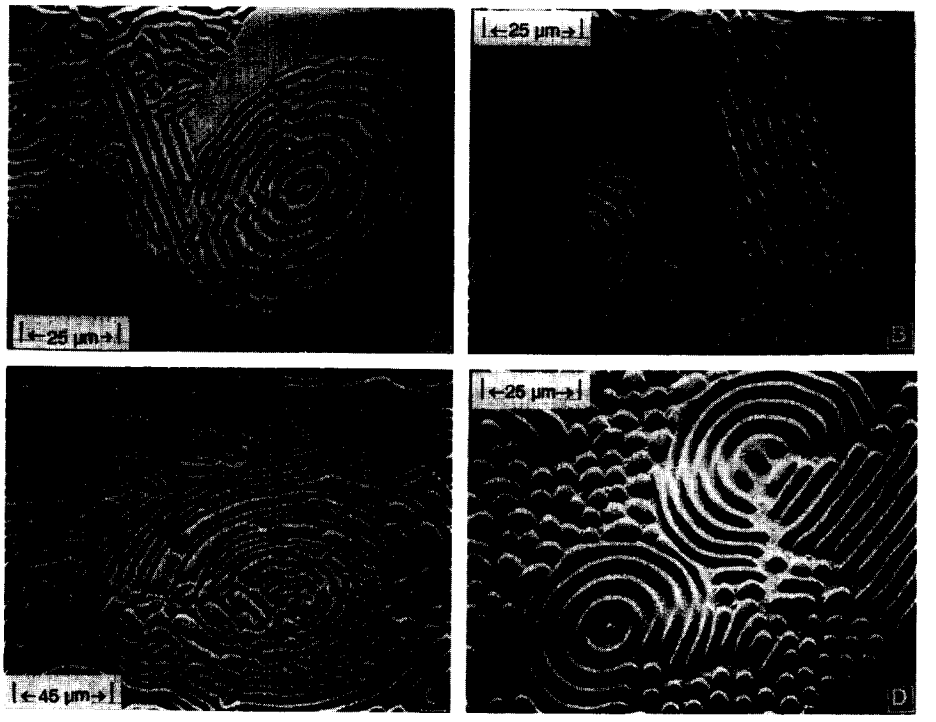

Fig. 5. (**A** through **D**) A selection of patterns formed during the dewetting of thin polystyrene films on a glass substrate, with a typical peak-to-valley height of 0.2 μm. The structure shown in (C) is typical of those formed close to the contact point.

tration and spinning speed were chosen to yield a film about 700 Å thick; it actually measured 710 Å (within 10 Å) by independent profilometry. The spin-coated film, checked by differential interference contrast microscopy (*12*), was uniform over the diameter of the lens (50 mm).

The optically smooth glass surface was a planoconvex lens with a radius of curvature of 1000 mm. This slight curvature caused the rigid glass transducer to be in point contact with the polystyrene film. In this way, we could follow the tunneling gap beyond where the topographic growth wet the transducer simply by moving radially from the contact point (the transducer and sample move together, independent of the microscope). This simple technique worked where many others had failed and has found general use for this class of sample.

The observations were made 2 mm away from the point of contact, a distance large compared with the thickness of the film. However, the point of contact, despite being far away from the area of observation, does indeed affect the structural evolution during the dewetting process. Detailed results are forthcoming (*49*).

When the polystyrene film is heated to above its glass transition temperature, a variety of patterns of ripples and periodic lines arises, and the merging of these structures, giving rise to droplets, is dramatically revealed with the PTM (Fig. 5). The structures at this stage are about 0.2-μm high and are highly periodic.

Figure 6 shows a time sequence of the dewetting process. The polystyrene film in this case was heated to 165°C, well above the glass transition temperature. Dewetting begins as formation of ripple-like structures, whose amplitude is on the order of a few nanometers at the start of the breakup and grows to a peak-to-peak height of 0.2 μm. The spacing between the ripples is typically about 5 μm. Several such ripples start at the same instant, leading to the observed structure.

Should the film break up by a spinodal decomposition mechanism, one would expect to find ripples or waves, as is observed, but one does not expect the ordered structure also seen here. The ripples eventually grow in amplitude and spatial extent, colliding with similar structures formed a distance away. Each filament of the polymer making up the ripple undergoes a Rayleigh-type instability, giving rise to discrete droplets. In time, the entire surface of the glass substrate is filled with little beads of the polymer.

We believe that this is the first direct observation of the path taken by a thin polymer film as it starts to dewet by a spinodal decomposition mechanism. The ripples are then attributed to the amplifications of thermal fluctuations before the dewetting of the film. We were concerned that the observed structure might be a result of a Rayleigh-Benard type instability, as there is a temperature gradient normal to the film plane (along the optic axis of the microscope). The situation then becomes identical to the case of a liquid film heated from below, giving rise to buoyancy-driven convection. In this case, above a certain critical temperature gradient, an instability attributable to convection is initiated. In the case of polymeric fluids, such instabilities do not occur because of the high viscosities involved (*50*). Hence, we attribute the observed structures to dewetting through a spinodal mechanism, rather than to a Rayleigh-Benard type instability.

Experiments with a polystyrene of higher molecular weight (M_w = 80,000; M_w/M_n < 1.04) reveal structures similar to those in Fig. 6. The circular, ripple-like structure does eventually break up into little droplets, as is expected (*46*) for a film breaking up by means of a spinodal decomposition process. It appears from the results presented that the film breaks up with a complicated mechanism that has characteristics of a spinodal decomposition and a nucleation and growth process.

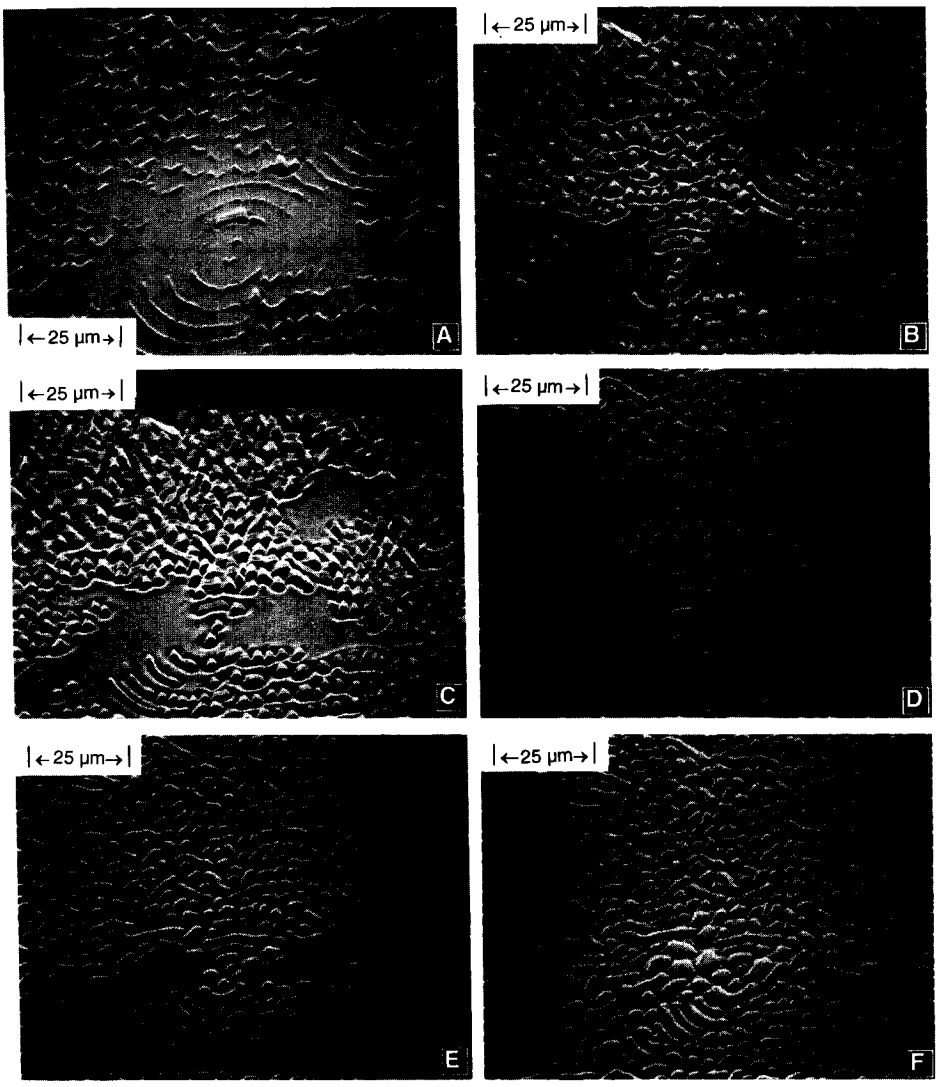

Fig. 6. A time sequence of the ripple structures as the polystyrene film starts to dewet: (**A**) 60 s, (**B**) 456 s, (**C**) 540 s, (**D**) 564 s, (**E**) 864 s, and (**F**) 1200 s. (C) and (D) were made almost simultaneously to show the demagnification made for clarity and to allow calibration over the entire sequence. Peak-to-valley height is typically 0.2 μm.

REFERENCES AND NOTES

1. B. W. Cherry, *Polymer Surfaces* (Cambridge Solid-State Science Series, Cambridge Univ. Press, Cambridge, 1981), pp. 100–103.
2. J. D. Miller and H. Ishida, in *Fundamentals of Adhesion*, L.-H. Lee, Ed. (Plenum, New York, 1991), chap. 10.
3. J. M. Guerra, *Appl. Opt.* **29**, 3741 (1990).
4. V. K. Berry, *Scanning* **10**, 19 (1988).
5. G. D. Danilatos, *J. Microsc.* **162**, 391 (1991).
6. G. Binnig, C. F. Quate, Ch. Gerber, *Phys. Rev. Lett.* **56**, 930 (1986).
7. D. W. Pohl, U. Ch. Fischer, U. T. Dürig, *Proc. SPIE* **897**, 84 (1988) and references therein.
8. E. Betzig and J. K. Trautman, *Science* **257**, 189

(1992) and references therein.
9. R. C. Reddick, R. J. Warmack, T. L. Ferrell, *Phys. Rev. B* **39**, 767 (1989).
10. G. Binning and H. Rohrer, *Surf. Sci.* **126**, nos. 1–3 (1983).
11. N. H. Hartshorne and A. Stuart, *Crystals and the Polarizing Microscope* (Arnold, London, ed. 4, 1970), chaps. 5 and 7.
12. P. Sullivan and B. Wunderlich, *Soc. Pet. Eng. Trans.* **4**, 2 (1964).
13. G. M. Robinson, D. M. Perry, R. W. Peterson, *Sci. Am.* **265**, 66 (July 1991).
14. C. J. R. Sheppard, in *Advances in Optical and Electron Microscopy*, R. Barer and V. E. Coslett, Eds. (Academic Press, London, 1987), vol. 10, pp. 1–98.
15. J. M. Guerra and W. T. Plummer, U.S. Patent 4,681,451 (1987).
16. J. M. Guerra, *Proc. SPIE* **1009**, 254 (1988).
17. C. W. McCutchen, *Rev. Sci. Instrum.* **35**, 1340 (1964).
18. E. J. Ambrose, *Nature* **178**, 1194 (1956).
19. W. Knoll, *MRS Bull.* **16**, 29 (1991).
20. I. Newton, *Opticks* (Dover, New York, 1979), part 1, pp. 193–224.
21. S. G. Lipson and H. Lipson, *Optical Physics* (Cambridge Univ. Press, Cambridge, ed. 2, 1981), pp. 384–386.
22. N. J. Harrick, *Internal Reflection Spectroscopy* (Harrick Scientific Corp., Ossing, NY, 1979), pp. 1–65.
23. J. Strong, *Concepts of Classical Optics* (Freeman, San Francisco, CA, 1958), pp. 124–126 and 516–518.
24. D. D. Coon, *Am. J. Phys.* **34**, 240 (1966).
25. D. Bohm, *Quantum Theory* (Prentice-Hall, Englewood Cliffs, NJ, 1951), p. 240.
26. J. M. Vigoureux, C. Girard, D. Courjon, *Opt. Lett.* **14**, 1039 (1989).
27. J. M. Vigoureux, F. Depasse, C. Girard, *Appl. Opt.* **31**, 3036 (1992).
28. S. Zhu, A. W. Yu, D. Hawley, R. Roy, *Am. J. Phys.* **54**, 601 (1986).
29. S. G. Lipson and H. Lipson, *Optical Physics* (Cambridge Univ. Press, London, 1969), pp. 79–109 and 282–285.
30. C. Ma and R. W. Smith, *Proc. SPIE* **1028**, 45 (1988).
31. K. Matsumoto and T. Tsuruta, *Opt. Eng.* **31**, 2657 (1992).
32. N. F. van Hulst, N. P. de Boer, B. Bölger, *J. Microsc.* **163**, 117 (1991).
33. H. G. Needham, *The Practical Use of The Microscope* (Thomas, Springfield, IL, 1958), pp. 144, 228–229, 254–255, and appendix E.
34. M. A. Winnik, Y. Wang, F. Haley, *J. Coatings Tech.* **64**, 51 (1992).
35. Y. Wang *et al.*, *Langmuir* **8**, 1435 (1992).
36. S. T. Eckersley and A. Rudin, *J. Coatings Tech.* **62**, 89 (1990).
37. M. Srinivasarao, R. S. Stein, T. P. Russell, J. M. Guerra, *Polymer*, in press.
38. A. Keller, *Philos. Mag.* **2**, 1171 (1957).
39. P. H. Till Jr., *J. Polym. Sci.* **24**, 301 (1957).
40. E. W. Fischer, *Z. Naturforsch.* **120**, 753 (1957).
41. A. Keller and A. O'Connor, *Discuss. Faraday Soc.* **25**, 114 (1958).
42. P. H. Geil, *Polymer Single Crystals* (Wiley-Interscience, New York, 1963), chap. 3.
43. G. F. Teletzke, H. T. Davis, L. E. Scriven, *Chem. Eng. Commun.* **55**, 41 (1987).
44. P. G. de Gennes, *Rev. Mod. Phys.* **57**, 827 (1985).
45. J. Daillant, J. J. Bennatar, L. Leger, *Phys. Rev. A* **41**, 1963 (1990).
46. F. Brochard-Wyart and J. Daillant, *Can. J. Phys.* **68**, 1084 (1990).
47. C. Redon, F. Brochard-Wyart, F. Rondelez, *Phys. Rev. Lett.* **66**, 715 (1991).
48. G. Reiter, *ibid.* **68**, 75 (1992).
49. M. Srinivasarao, R. S. Stein, J. M. Guerra, T. P. Russell, in preparation.
50. R. G. Larson, *Rheol. Acta* **31**, 213 (1992).
51. The authors wish to thank T. Russell, R. Larson, H. Winter, G. Berry, and W. T. Plummer for many helpful discussions. We further acknowledge the support of the Polaroid Corp. and the National Science Foundation (DMR-9101323).